

# Segmentation of nearly isotropic overlapped tracks in photomicrographs using successive erosions as watershed markers

Alexandre Fioravante de Siqueira<sup>a,b,\*</sup>, Wagner Massayuki Nakasuga<sup>a</sup>, Sandro Guedes<sup>a</sup>, Lothar Ratschbacher<sup>b</sup>

<sup>a</sup>*Departamento de Raios C3smicos e Cronologia, IFGW, University of Campinas*

<sup>b</sup>*Institut f3ur Geologie, TU Bergakademie Freiberg*

---

## Abstract

The major challenges of automatic track counting are distinguishing tracks and material defects, identifying small tracks and defects of similar size, and detecting overlapping tracks. Here we address the latter issue using WUSEM, an algorithm which combines the watershed transform, morphological erosions and labeling to separate regions in photomicrographs. WUSEM shows reliable results when used in photomicrographs presenting almost isotropic objects. We tested this method in two datasets of diallyl phthalate (DAP) photomicrographs and compared the results when counting manually and using the classic watershed. The mean automatic/manual efficiency ratio when using WUSEM in the test datasets is  $0.97 \pm 0.11$ .

*Keywords:* Automatic counting, Diallyl phthalate, Digital image processing, Fission track dating

---

---

\*Corresponding author. Phone: +55(19)3521-5362.

*Email addresses:* [siqueiraaf@gmail.com](mailto:siqueiraaf@gmail.com) (Alexandre Fioravante de Siqueira), [wamassa@gmail.com](mailto:wamassa@gmail.com) (Wagner Massayuki Nakasuga), [sguedes@ifi.unicamp.br](mailto:sguedes@ifi.unicamp.br) (Sandro Guedes), [lothar.ratschbacher@geo.tu-freiberg.de](mailto:lothar.ratschbacher@geo.tu-freiberg.de) (Lothar Ratschbacher)

*Authorship statement:* A. F. de S. designed the algorithms, wrote the code, analyzed the data and wrote the paper. W. M. S. counted the tracks in the images, analyzed the data and wrote the paper. S. G. obtained the images from the samples, analyzed the data, wrote the paper and supervised the research project. L. R. supervised the research project.

## 1. Introduction

Solid state nuclear track detectors (SSNTD) are materials such as inorganic crystals, plastics and glasses, known to record the path of charged particles. There are several applications for SSNTD in nuclear science; for instance, measurements of radon gas [1], boron neutron capture therapy [2], and age determination by fission track dating [3, 4, 5, 6, 7, 8].

When a charged particle collide in a SSNTD, the ionization and/or the collision with atoms modify the path by which the particle go through. This damage in the SSNTD structure is called latent track. This track becomes visible under an optical microscope after a convenient etching process [9], and these tracks can be counted. Photomicrographs can also be used, which could improve the counting accuracy [10].

Procedures for measuring and counting tracks are time-consuming and involve practical problems, e.g. variation in observer efficiency [11]. An automatic method based on image processing techniques could increase the track counting rate and improve counting reproducibility. However, separating elements in nontrivial images is one of the hardest tasks in image processing [12].

Automatic systems for separating, counting or measuring tracks have been studied for a while, and several solutions were presented (e.g. [13, 14, 15, 16, 17, 18, 19, 20, 21, 22, 23, 24, 25, 26, 27, 11, 28, 29]). Still, the precision of automatic methods is not satisfactory yet; an automatic analysis could need to be manually adjusted by the operator, being more time consuming than the usual measure [26, 30]. The major challenges to automatic track counting are detecting overlapping tracks, distinguishing tracks and material defects (e.g. surface scratches due to polishing), and identifying small tracks and defects of comparable size in the background of photomicrographs [11].

To address the problem of identifying overlapping ion tracks in photomicrographs, we propose an algorithm based on the watershed transform [31] using morphological erosions [32] as markers. A similar method was used to separate packings of ellipsoidal particles represented using X-Ray tomography [33].

We tested this method in two datasets of diallyl phthalate (DAP) photomicrographs, and used the results to relate the incident track energy with the mean gray levels and mean diameter products for each sample from the first dataset.

## 2. Material and methods

We employed the ISODATA threshold to obtain the binary images used in our tests. The WUSEM algorithm is based on the following techniques: 1. morphological erosion; 2. watershed transform, and 3. labeling. We describe these algorithms in this Section.

### 2.1. The ISODATA threshold

The Iterative Self-Organizing Data Analysis Technique (A) (ISODATA) threshold [34, 35] is an histogram-based method. It returns a threshold that separates the image into two pixel classes, where the threshold intensity is halfway between their mean intensities.

When applied for two classes, ISODATA is always convergent [36]; in our case, these classes are the tracks (our regions of interest, ROI) and the background. We used the algorithm `filters.threshold_isodata`, implemented in `scikit-image` [37].

### 2.2. Structuring elements and morphological erosion

In morphological image processing, a structuring element is a matrix representing a mask, or a shape, that is used to retrieve information about the shapes in an input image [32]. Erosion, a basic operation in image processing, uses a chosen structuring element to shrink the border of all ROI in a binary image; the shrinkage factor is correspondent to the structuring element size [12].

In our tests (Section 3) we used disks as structuring elements, since tracks in DAP are mostly round in shape. The algorithms used were `morphology.disk` and `morphology.erosion`, contained in `scikit-image`.

### 2.3. Watershed transform

The watershed algorithm is a non-parametric method which defines the contours as the watershed of the gradient modulus of the gray levels of the input image, considered as a relief surface detection method [31].

In this algorithm, the input image is seen in a three-dimensional perspective. Two dimensions correspond to spatial coordinates, and the third represents the gray levels. In this interpretation, we consider three kinds of points [12]:

1. Points in regional minima.
2. Points where a drop of water would flow to a common minimum.
3. Points where a drop of water would flow to different minima. The set of these points is named *watershed line*.

The aim of watershed algorithms is to find the watershed lines. The method used in this paper is implemented in the function `morphology.watershed`, from `scikit-image`.

### 2.4. Labeling algorithm

In image processing, the labeling algorithm labels connected regions of a binary input image, according to the 2-connectivity sense: all eight pixels surrounding the reference pixel. Pixels receive the same label when they are connected and have the same value. We used the algorithm `measure.label` from `scikit-image`, implemented as described in [38].

### 2.5. Watershed Using Successive Erosions as Markers (WUSEM) algorithm

Here we present the WUSEM (Watershed Using Successive Erosions as Markers) algorithm, which combines morphological erosions, the watershed transform and labeling algorithms to separate regions of interest (ROI) in binary images. The WUSEM algorithm and its steps follow (Figure 1):

1. The user define an initial radius ( $r_0$ ) and an iterative radius ( $\Delta r$ ) to a structuring element (Figure 2).

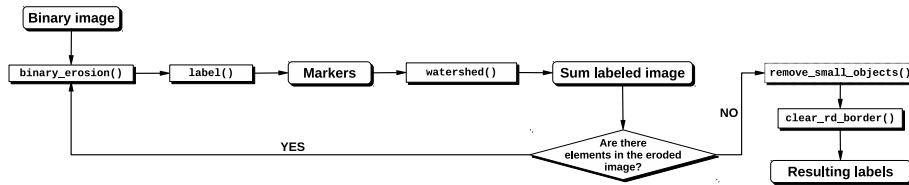


Figure 1: Representing WUSEM and the functions employed in its implementation.

2. The input binary image is eroded using the structuring element with radius equal to  $r_0$ . This erosion is used as a marker to the watershed algorithm. Then, the resulting image is labeled. This is the first segmentation.
3. A new structuring element is defined. Its radius is  $r_0 + \Delta r$ . The input binary image is eroded with this new structuring element, the erosion is used as a marker to watershed, and the result is labeled. This is the second segmentation.
4. The process continues until the eroded image does not have objects. Then, all segmentations are summed.
5. The result is labeled again, to reorder the ROI, and labels with area smaller than 64 pixels are excluded, to ensure that noise will not affect the results. Tracks are counted according to the “lower right corner” method, where objects that touch the bottom and right edges are not counted. This leads to an accurate, unbiased measure [39].

WUSEM is implemented in the function `segmentation_wusem()`, available in the Supplementary Material. It receives the arguments `str_el`, `initial_radius` and `delta_radius`, representing the structuring elements,  $r_0$  and  $\Delta r$ , respectively. To exemplify WUSEM’s capabilities, we used it to separate overlapping tracks within the test photomicrographs (Figure 3).

### 2.6. DAP photomicrographs

We used two sets of diallyl phthalate (DAP,  $C_{14}H_{14}O_4$ ) photomicrographs to test the WUSEM algorithm. One of them was obtained from detectors irradiated with  $^{78}Kr$  tracks, and the other has induced fission tracks.

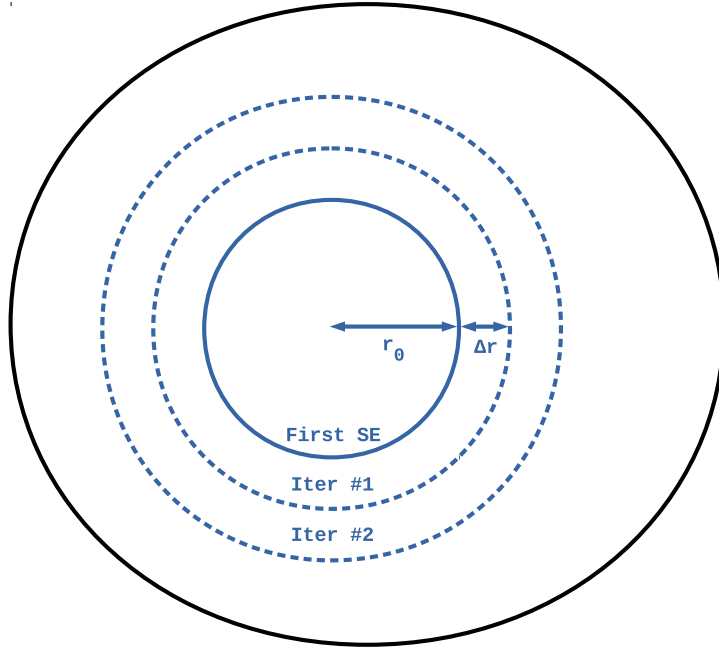


Figure 2: Representation of disks as structuring elements defined for each segmentation when employing WUSEM in an interest region. The radius of the first, second and third structuring elements are  $r_0$ ,  $r_0 + \Delta r$  and  $r_0 + 2\Delta r$ , respectively.

### 2.6.1. $^{78}\text{Kr}$ tracks

The first dataset contains 362 photomicrographs of tracks from nine different DAP plaques irradiated with  $^{78}\text{Kr}$  ions at a nominal fluence of  $1.4 \times 10^5 \text{ cm}^{-2}$ , from a beam perpendicular to the detector surfaces at GSI, Darmstadt, Germany<sup>2</sup>.

During the irradiation, detectors were covered with aluminum foils forming a moderation layers of thicknesses varying from zero (no cover) to  $90 \mu\text{m}$ . Detectors were named after their cover thicknesses (K0, K20, K30, ..., K90). Ions arrived at the setup with initial energy of 865 MeV and were slowed down in the aluminum cover before hitting the detector surface. Incidence energies were

---

<sup>2</sup>These photomicrographs are contained in the folder `orig_figures/dataset_01`, available in the Supplementary Material.

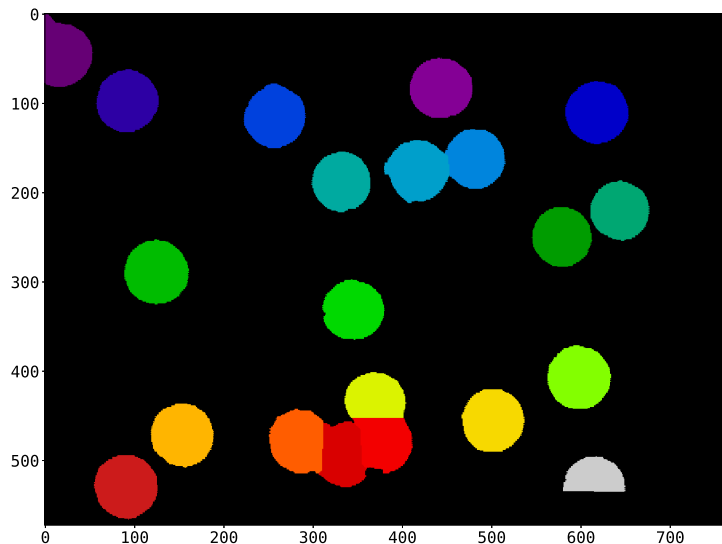


Figure 3: WUSEM algorithm application in an input image. First, the image is binarized using the ISODATA threshold. Then, the image is eroded using initial radius ( $r_0$ ) and iterative radius ( $\Delta r$ ) equal to 1 and 1 respectively, to ease visualization. The process continues until the eroded image has regions in it. All erosions are summed, and the result is labeled; then, regions with area smaller than 64 px are excluded. Each labeled track receives a color from the `nipy_spectral` colormap. Finally, the function `enumerate_objects()` is used to number the found tracks. Final results are shown to  $r_0$  and  $\Delta r$  equal to 10 and 4, respectively. Animation also available at <https://youtu.be/CtI0xhNISW8>.

calculated using the software SRIM [40], and varied from 18 MeV ( $90 \mu\text{m}$  cover) to 865 MeV (no cover). Detectors were etched in a PEW solution (7.5 g KOH, 32.5 g ethanol, 10 g water) solution for  $4.5 \pm 0.2$  min at  $65 \pm 3^\circ\text{C}$ .

Images were captured with a CCD camera coupled with a Zeiss microscope, in reflected light mode, under  $1250 \times$  nominal magnification. Then, the detectors were further etched for 4 minutes, total of  $8.5 \pm 0.3$  min, and new images were captured. This way, we obtained 18 subsets of images. Tracks within these photomicrographs are almost isotropic and have the same orientation, resembling circles (Figure 4).

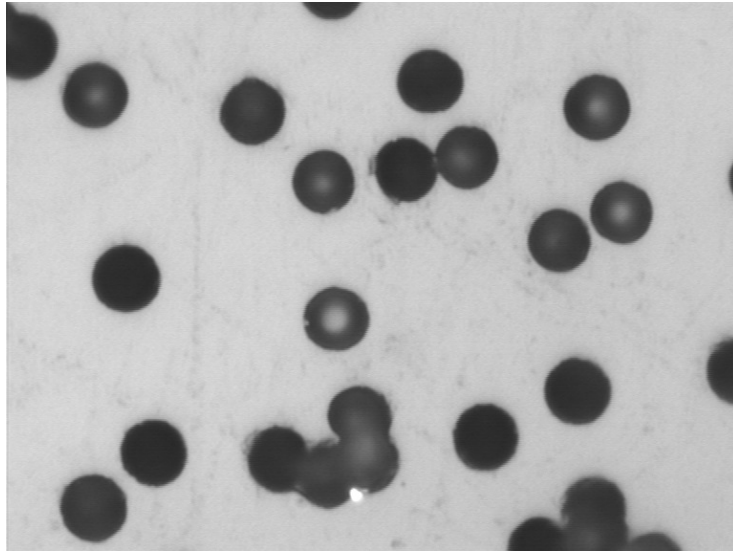


Figure 4: Photomicrograph from the first dataset, presenting tracks in a DAP sample.

### 2.6.2. Induced fission tracks

The second dataset contains 19 photomicrographs with two different magnifications from a DAP plaque used as external detector, coupled to an apatite sample and irradiated with thermal neutrons to induce fission in the  $^{235}\text{U}$  atoms inside the mineral<sup>3</sup>. During the fission process, two fragments are released and, eventually, are detected by the DAP plaque. Fragments arrive at the detector surface with different energies and incidence angles, resulting in a variety of track formats. Hence, counting tracks in these photomicrographs is more complex than in the previous case (Figure 5).

### 2.7. License and reusability

The WUSEM algorithm and several functions for its implementation lie within the packages Numpy [41], Scipy [42], Matplotlib [43], scikit-image [37], among others. All code published with this paper is written in Python 3 [44]

---

<sup>3</sup>These photomicrographs are contained in the folder `orig_figures/dataset_02`, available in the Supplementary Material.

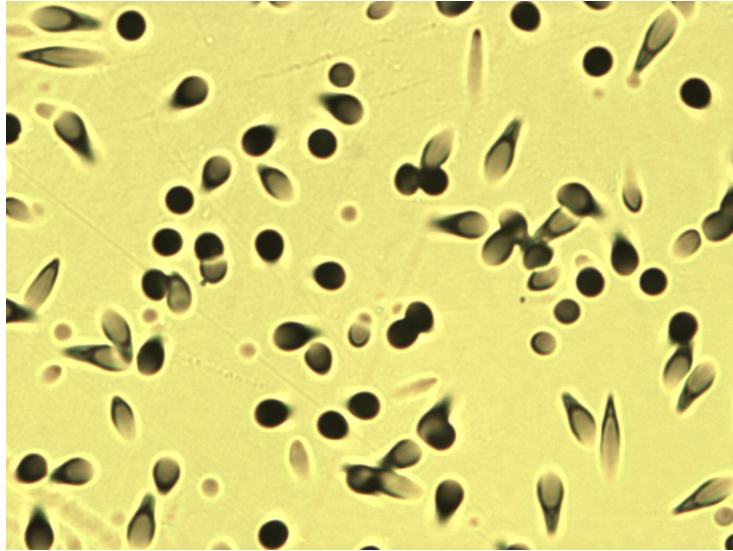


Figure 5: Input test photomicrograph from the second dataset, presenting tracks in a DAP sample.

and is available under the GNU GPL v3.0 license, and all photomicrographs and figures distributed with this paper are available under the CC-BY 2.0 license.

### 3. Experimental

#### 3.1. Processing photomicrographs of $^{78}\text{Kr}$ tracks

##### 3.1.1. Exemplifying the methodology

Here we use a photomicrograph from the first dataset<sup>4</sup> to exemplify WUSEM (Figure 4). We binarized this photomicrograph using the ISODATA threshold [34, 35] (Figure 6). Different gray levels in some tracks may not be properly separated, complicating the extraction of track features. To address this issue, we filled the regions in the binary image using the function `ndimage.morphology.binary_fill_holes()` from `scipy`.

---

<sup>4</sup>Image `K90_incid4,5min.3.bmp` from the folder `orig_figures/dataset.01/Kr-78.4,5min/K90_incid`, available in the Supplementary Material.

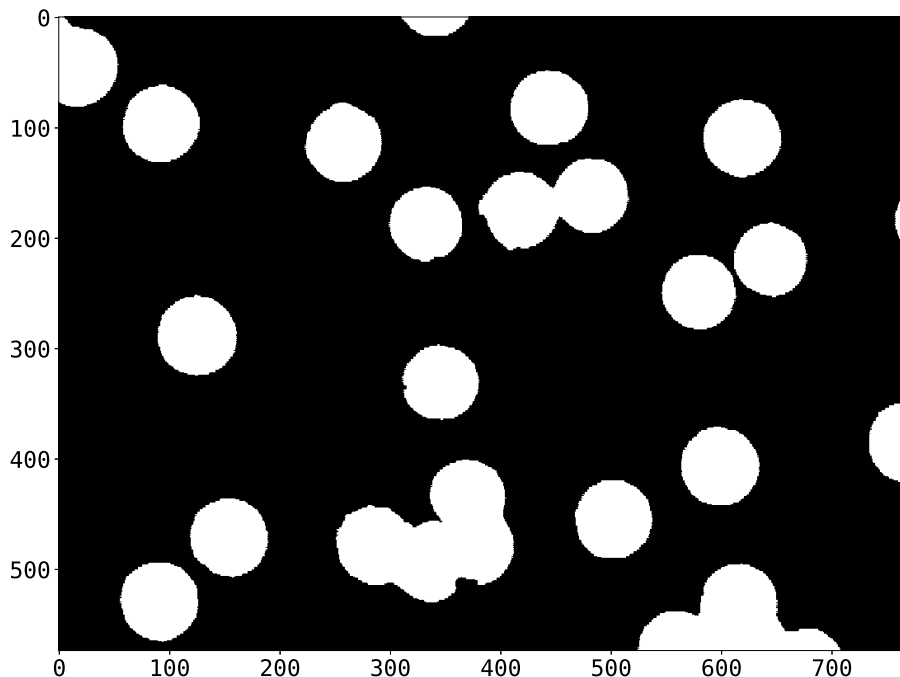


Figure 6: Input photomicrograph (Figure 4) binarized using the ISODATA threshold (threshold = 128) and region filling. Colormap: `gray`.

After binarizing the input image, the WUSEM algorithm separates the overlapping tracks (Figure 7). For this example, we chose `initial_radius = 10` and `delta_radius = 4` as parameters.

Tracks were counted using the “lower right corner” method, i.e., border tracks are only counted if they lie on the right or bottom edges of the image. We used the function `clear_rd_border()`, given in the Supplementary Material, to remove the tracks in these edges. WUSEM returns a labeled region, which can be used as parameter to the function `enumerate_objects()` (Figure 8).

### 3.1.2. Comparison between manual and automatic counting

An experienced observer can easily distinguish tracks in the photomicrograph, even when several tracks are superimposed. For this reason, manual counting is considered the control in the comparison with the automatic count-

ing. In the following, the WUSEM algorithm is applied to the photomicrograph set and the processing parameters are studied.

We established an arbitrary value of up to two tracks less than the mean of the manual counting as a tolerance. WUSEM's parameters become candidates if the automatic counting lies within the tolerance interval, i.e.  $0 < \mu_{n_{\text{manual}}} - n_{\text{auto}} < 2$ , where  $n$  is the track number obtained by each approach (Figure 9).

WUSEM's best parameters for this study are the ones within the tolerance interval for most samples. According to the stated comparison, the best parameters are `initial_radius = 10`, `delta_radius = 20` for 4.5 min samples, and `initial_radius = 10`, `delta_radius = 14` for 8.5 min samples.

Using the best parameters defined, we compared manual, classic (flooding) watershed and WUSEM counting for each sample (Figure 10, Table 1). The classic watershed algorithm used is implemented in ImageJ [45], and the full method consisted in binarizing the input image, applying the watershed and removing small objects. The source code for these operations and instructions on how to use it are given in the Supplementary Material.

Since tracks in this dataset have the same shapes, we can attribute an efficiency of 100 % for manual counting. WUSEM counting was initially set to obtain a smaller number of tracks when compared to the manual counting. However, WUSEM counting returns false positives, i.e., incorrectly labels background regions as ROI (points above the 1:1 line in Figure 10 (b) and (d)). To avoid false positives, one could use a more restrictive criterion, such as eccentricity (Section 3.1.3).

Counting reproducibility is important for considering the reliability of track counting. Despite the variations in track characteristics, the efficiencies of WUSEM's automatic counting remained constant within uncertainties, when compared to manual counting.

Sample	Manual counting ( $\mu \pm 1\sigma$ )		WUSEM counting ( $\mu \pm 1\sigma$ )		Efficiency $\pm 1\sigma$	
	4.5 min	8.5 min	4.5 min	8.5 min	4.5 min	8.5 min
<b>K0</b>	22 $\pm$ 3	20 $\pm$ 3	21 $\pm$ 2	19 $\pm$ 3	0.99 $\pm$ 0.12	0.95 $\pm$ 0.11
<b>K20</b>	25 $\pm$ 5	22 $\pm$ 4	23 $\pm$ 3	22 $\pm$ 3	0.90 $\pm$ 0.11	0.99 $\pm$ 0.14
<b>K30</b>	23 $\pm$ 4	24 $\pm$ 4	22 $\pm$ 4	22 $\pm$ 3	0.96 $\pm$ 0.12	0.94 $\pm$ 0.10
<b>K40</b>	22 $\pm$ 4	22 $\pm$ 4	22 $\pm$ 3	21 $\pm$ 3	1.01 $\pm$ 0.10	0.96 $\pm$ 0.08
<b>K50</b>	24 $\pm$ 2	22 $\pm$ 4	23 $\pm$ 3	20 $\pm$ 3	0.94 $\pm$ 0.11	0.95 $\pm$ 0.13
<b>K60</b>	25 $\pm$ 3	23 $\pm$ 4	25 $\pm$ 3	22 $\pm$ 3	0.99 $\pm$ 0.08	0.97 $\pm$ 0.13
<b>K70</b>	21 $\pm$ 4	17 $\pm$ 4	21 $\pm$ 4	17 $\pm$ 4	1.00 $\pm$ 0.07	1.00 $\pm$ 0.13
<b>K80</b>	21 $\pm$ 4	20 $\pm$ 5	20 $\pm$ 4	20 $\pm$ 4	0.96 $\pm$ 0.13	1.02 $\pm$ 0.14
<b>K90</b>	24 $\pm$ 4	21 $\pm$ 4	23 $\pm$ 4	21 $\pm$ 4	0.99 $\pm$ 0.11	0.94 $\pm$ 0.09

Table 1: Mean, standard deviation, and automatic/manual efficiency ratio for each sample of the first dataset.

### 3.1.3. Relating ion energies with diameter product and mean gray levels

In this application, we use WUSEM to relate the track energies to the product of major and minor diameters ( $D_>$  and  $D_<$ , respectively) and the mean gray level of each track. We considered only approximately circular tracks in our analysis, based on an eccentricity ( $\epsilon$ )<sup>5</sup> criterion:  $\epsilon$  should be equal to or less than 0.3 (Figure 11). This additional criterion can be used also for counting tracks, to ensure that false positives (spurious objects counted as tracks) are avoided.

After separating each track, we can obtain its features such as gray levels and diameters. Once the mean gray level and diameters of each track in a photomicrograph are obtained, we can relate them with the incident energy for each sample. The mean gray level of each sample is obtained getting the mean of all gray levels of the tracks in the images of that sample. We adopted a similar process to obtain the mean diameters. Then, the results are related to the incident energy (Figure 12).

The diameter products roughly reflect the electronic energy loss (dE/dx) curve for  $^{78}Kr$  in DAP (Figure 12 (a) and (c)), calculated with the software

<sup>5</sup>In image processing, the eccentricity of an object is a number in the interval  $[0, 1)$ . The lower the value, the region becomes closer to a circle.

SRIM [40]. The Bragg peak appears around 100 MeV. Further scatter of points can be attributed to poor control of etching conditions. The uncertainty of 3 °C in temperature may cause a large variation in etching results [46]. Variations in gray level means are impaired probably because this set was acquired in reflected illumination mode, which privileges surface details over depth effects.

### 3.2. Processing photomicrographs of fission tracks in DAP

In photomicrographs from the first dataset, our main concern was track superposition. However, all tracks were similar, created by a collimated beam of  $^{78}\text{Kr}$  tracks. Here we go one step ahead, applying WUSEM to images where tracks present a variety of shapes. This image dataset was obtained from DAP plaques irradiated with thermal neutrons, coupled with apatite mounts. Fission fragments are born in the interior of the mineral, then emitted at different directions towards the detector. For instance, round tracks were created by perpendicular incident fragments, while the elliptical ones were created by particles hitting DAP surface at shallower angles (Figure 5).

As in the previous analysis, the manual counting performed by an experienced observer is taken as reference because we expect the observer to be able to recognize tracks efficiently. However, in this case, we do not expect the observer efficiency to 100 %. Fragments hitting the detector at lower energies originate tracks that are very difficult to distinguish from detector surfaces. An experienced observer would avoid counting those tracks to keep hers/his counting efficiency constant.

Repeating the previous processes for photomicrographs in the second dataset, we first binarize a test photomicrograph<sup>6</sup> (Figure 5) using the ISODATA threshold. The binarized image is generated for two scenarios: considering and ignoring border tracks. Here, regions in the binary image are also filled using the function `ndimage.morphology.binary_fill_holes()` from `scipy`. Then we apply

---

<sup>6</sup>Image “FT-Lab.19.07.390.MAG1.jpg”, from the folder `orig_figures/dataset.02`. Available in the Supplementary Material.

the WUSEM algorithm. We chose `initial_radius = 5` and `delta_radius = 2` as parameters, and the WUSEM result as parameter in the function `enumerate_objects()` (Figure 13).

For this dataset, we established an arbitrary tolerance of five tracks less than the mean of the manual counting. In this case, WUSEM’s parameters become candidates if  $0 < \mu_{n_{manual}} - n_{auto} < 5$ , where  $n$  is the track number obtained by each approach. According to the stated comparison, the best parameters are `initial_radius = 5`, `delta_radius = 12` for the first magnification and `initial_radius = 10`, `delta_radius = 14` for the second one. Using the best parameters defined, we compared manual, classic watershed and WUSEM counting for each sample (Figure 14, Table 2).

Magnification	Manual counting ( $\mu \pm 1\sigma$ )	WUSEM counting ( $\mu \pm 1\sigma$ )	Efficiency $\pm 1\sigma$
<b>1</b>	85 $\pm$ 8	83 $\pm$ 6	0.98 $\pm$ 0.07
<b>2</b>	37 $\pm$ 3	37 $\pm$ 5	0.99 $\pm$ 0.05

Table 2: Mean, standard deviation, and automatic/manual efficiency ratio for each magnification of the second dataset.

WUSEM succeeded in avoiding false positives in this application, when compared to the classic watershed (black line above the 1:1 line in Figure 14 (b)). Still, the user could apply more restrictive criteria. Also, it is worth noting the efficiency variation between the two image sets. Bigger objects are easier to be treated, thus automatic track counting in greater magnification images resulted in a higher counting efficiency (Table 2).

## 4. Discussion

### 4.1. Structuring elements

In this study, we used disks as structuring elements for processing images in both datasets. Since tracks in photomicrographs from dataset 1 are almost isotropic (as seen in Figure 4), disks are suitable structuring elements to be used in their segmentation. However, tracks within images in dataset 2 do not have a defined format (Figure 5). Employing different structuring elements, e.g.

rotated cones or ellipses, could improve their segmentation and the automatic counting result.

#### *4.2. False positives, false negatives and counting efficiency*

In track counting, reproducibility is not about counting every track in the image, but counting the same types of tracks every time. It is the primary concern in FTD: for instance, the efficiencies for counting tracks in the standard sample should not vary when using zeta age calibrations [47, 48]. For absolute methods of determining neutron fluence [49], the efficiency should be constant when counting tracks in unknown age samples. The fast-growing areas of FTD using the Laser Ablation Inductively Couple Plasma Mass Spectrometer (LA-ICP-MS, [50, 51, 52, 53]) or the Electron Microprobe ([54, 55]) have the same efficiency issues, and could also benefit from automatic counting.

The major challenge for reproducibility is avoiding false positives, spurious objects such as scratches on the detector or mineral surface and other etching figures which automatic counting algorithms could misrepresent as tracks. In most situations, it is preferable to restrict the criteria, thus increasing the number of false negatives (not counted tracks), even implying in efficiency reduction.

Even more experienced observers expect some decreasing in efficiency due to superposition when counting tracks in high track density samples. This loss tends to be more severe in automatic counting. When applying algorithms as WUSEM, the separation of tracks in objects formed of several tracks is not always possible.

Counting less tracks than the actual number in a cluster is acceptable; however, when processing a large number of clusters in higher track density samples, we expect a lower efficiency when compared with lower track density samples. This effect can be assessed by calibrating the efficiency as a function of track density. Therefore, efficiencies presented for WUSEM (Tables 1 and 2) only hold for the track densities of the used samples.

#### 4.3. Perspective of future development

The WUSEM algorithm represents an advance in automated track counting, opening several possibilities. Differently from the direct application of classic watershed, WUSEM allows adaptation (Figure 15): the user can determine optimal structuring elements and efficiencies using a training image subset and apply these parameters to hers/his sample photomicrographs. This is very convenient in fission track dating, where the tracks present the same shapes regardless of the track source, and efficiency may vary mainly due to superposition of tracks in higher track density samples.

Another possibility is applying WUSEM in separate parts of the input image, allowing the determination of specific parameters for each track configuration. This could bring even better results when dealing with the superposition of two, three or more tracks.

## 5. Conclusion

In this paper we present a watershed algorithm using successive erosions as markers, which we call WUSEM. We employ WUSEM to separate overlapping tracks in photomicrographs. WUSEM performs well in images containing overlapping circular tracks (from a  $^{78}\text{Kr}$  collimated beam) and in photomicrographs with fission tracks at various orientations, both in DAP. The results are encouraging: the mean automatic/manual counting efficiency ratio is  $0.97 \pm 0.11$  when using WUSEM in the test datasets. We show also that diameter and eccentricity criteria may be used to increase the reliability of this method.

Since WUSEM using circles as structuring elements is aimed to isotropically shaped regions, this technique is suitable for separating etched tracks in DAP. Etching velocity in mineral surfaces depends on the crystal orientation, yielding more complex etching figures. Also, natural minerals are richer in scratches and other etching figures that can be mistaken with fission tracks, especially when using image processing techniques. WUSEM could be studied to separate tracks

in mineral surfaces; for that, it would need to use different structuring elements, which have to consider the orientation and shape of each track.

### **Acknowledgements**

The authors would like to thank Raymond Jonckheere for the second photomicrograph dataset and Matthias Schröter for his insights, and also Christina Trautmann for the sample irradiation at GSI in Darmstadt. This work is supported by the São Paulo Research Foundation (FAPESP), grants # 2014/22922-0 and 2015/24582-4.

### **Supplementary Material**

The supplementary material contains the complementary results and the code published with this study, and is available at [https://github.com/alexandrejaguar/publications/tree/master/2017/dap\\_segmentation](https://github.com/alexandrejaguar/publications/tree/master/2017/dap_segmentation).

### **References**

### **References**

- [1] J. M. C. Brown, S. Solomon, R. A. Tinker, Development of an energy discriminate CR-39® nuclear track etch dosimeter for Radon-220 gas measurements, *Journal of Environmental Radioactivity* 102 (10) (2011) 901–905. doi:10.1016/j.jenvrad.2010.09.008.
- [2] B. Smilgys, S. Guedes, M. Morales, F. Alvarez, J. C. Hadler, P. R. P. Coelho, P. T. D. Siqueira, I. Alencar, C. J. Soares, E. A. C. Curvo, Boron thin films and CR-39 detectors in BNCT: A method to measure the  $^{10}\text{B}(n,\alpha)^7\text{Li}$  reaction rate, *Radiation Measurements* 50 (2013) 181–186. doi:10.1016/j.radmeas.2012.07.001.  
URL <http://dx.doi.org/10.1016/j.radmeas.2012.07.001>

- [3] G. A. Wagner, P. Van den Haute, Fission-Track Dating, Springer Netherlands, Dordrecht, 1992. doi:10.1007/978-94-011-2478-2.  
URL <http://link.springer.com/10.1007/978-94-011-2478-2>
- [4] Y. Goto, T. Danhara, Zircon Fission-track Dating of the Hiyoriyama Cryptodome at Kuttara Volcano, Southwestern Hokkaido, Japan, Bulletin of the volcanological society of Japan 56 (1) (2011) 19–23. doi:10.18940/kazan.56.1\_19.
- [5] T. Imayama, T. Takeshita, K. Yi, D.-L. Cho, K. Kitajima, Y. Tsutsumi, M. Kayama, H. Nishido, T. Okumura, K. Yagi, T. Itaya, Y. Sano, Two-stage partial melting and contrasting cooling history within the Higher Himalayan Crystalline Sequence in the far-eastern Nepal Himalaya, Lithos 134-135 (2012) 1–22. doi:10.1016/j.lithos.2011.12.004.  
URL <http://linkinghub.elsevier.com/retrieve/pii/S002449371100377X>
- [6] H. Takagi, K. Tsutsui, H. Arai, H. Iwano, T. Danhara, Geological framework and fission track dating of pseudotachylyte of the Atotsugawa Fault, Magawa area, central Japan, Island Arc 22 (3) (2013) 318–337. doi:10.1111/iar.12036.  
URL <http://doi.wiley.com/10.1111/iar.12036>
- [7] T. Yuguchi, S. Sueoka, H. Iwano, T. Danhara, M. Ishibashi, E. Sasao, T. Nishiyama, Spatial distribution of the apatite fission-track ages in the Toki granite, central Japan: Exhumation rate of a Cretaceous pluton emplaced in the East Asian continental margin, Island Arc 26 (6) (2017) 1–15. doi:10.1111/iar.12219.  
URL <http://doi.wiley.com/10.1111/iar.12219>
- [8] T. Ninomiya, S. Taniguchi, S. Shimoyama, K. Watanabe, T. Danhara, H. Iwano, D. J. Dunkley, K. Shiraishi, C. Gouzu, U-Pb and fission-track dating of a submarine pyroclastic rock from southwest Japan, Island Arc

26 (6) (2017) 1–11. doi:10.1111/iar.12215.

URL <http://doi.wiley.com/10.1111/iar.12215>

- [9] R. L. Fleischer, P. B. Price, R. M. Walker, E. L. Hubbard, Track Registration in Various Solid-State Nuclear Track Detectors, *Physical Review* 133 (5A) (1964) A1443–A1449. doi:10.1103/PhysRev.133.A1443.  
URL <https://link.aps.org/doi/10.1103/PhysRev.133.A1443>
- [10] K. Moriwaki, Y. Shimpuku, M. Makimura, Improvement of Track Counting Accuracy and Efficiency in the Fission Track Method., *Radioisotopes* 47 (8) (1998) 611–616. doi:10.3769/radioisotopes.47.611.  
URL [https://www.jstage.jst.go.jp/article/radioisotopes1952/47/8/47\\_8\\_611/\\_article](https://www.jstage.jst.go.jp/article/radioisotopes1952/47/8/47_8_611/_article)
- [11] A. J. W. Gleadow, S. J. Gleadow, D. X. Belton, B. P. Kohn, M. S. Krochmal, R. W. Brown, Coincidence mapping - a key strategy for the automatic counting of fission tracks in natural minerals, *Geological Society, London, Special Publications* 324 (1) (2009) 25–36. doi:10.1144/SP324.2.  
URL <http://sp.lyellcollection.org/lookup/doi/10.1144/SP324.2>
- [12] R. C. Gonzalez, R. E. Woods, *Digital Image Processing*, 3rd Edition, Pearson, Upper Saddle River, NJ, USA, 2007.
- [13] D. Azimi-Garakani, J. G. Williams, Automatic fission track counting using the Quantimet 720, *Nuclear Instruments and Methods* 147 (1977) 69–73.
- [14] J. Beer, J. Pipper, W. Heinrich, Automatic measurements of nuclear tracks in plastic foils, *Journal of Physics E: Scientific Instruments* 15 (4) (1982) 439–443.  
URL <http://stacks.iop.org/0022-3735/15/i=4/a=013>
- [15] P. B. Price, W. Krischer, Semi-automated, three-dimensional measurement of etched tracks in solid-state nuclear track detectors, *Nuclear Instruments and Methods in Physics Research Section A: Accelerators, Spectrometers, Detectors and Associated Equipment* 234 (1) (1985) 158–167.

- [16] W. Trakowski, B. Schöfer, J. Dreute, S. Sonntag, C. Brechtmann, J. Beer, H. Drechsel, W. Heinrich, An automatic measuring system for particle tracks in plastic detectors, *Nuclear Instruments and Methods in Physics Research* 225 (1) (1984) 92–100. doi:10.1016/0167-5087(84)91342-5.
- [17] S. Masumoto, K. Wadatsumi, Computerized Image-Processing System for Fission-Track Dating, *Geoinformatics* 1 (1) (1990) 93–102.
- [18] K. Wadatsumi, S. Masumoto, Three-dimensional measurement of fission-tracks: Principles and an example in zircon from the Fish Canyon tuff, *International Journal of Radiation Applications and Instrumentation. Part D. Nuclear Tracks and Radiation Measurements* 17 (3) (1990) 399–406. doi:10.1016/1359-0189(90)90063-4.  
URL <http://linkinghub.elsevier.com/retrieve/pii/1359018990900634>
- [19] A. P. Fews, Fully automated image analysis of etched tracks in CR-39, *Nuclear Instruments and Methods in Physics Research Section B: Beam Interactions with Materials and Atoms* 71 (4) (1992) 465–478. doi:10.1016/0168-583X(92)95367-Z.  
URL <http://linkinghub.elsevier.com/retrieve/pii/0168583X9295367Z>
- [20] N. Petford, J. A. Miller, Three-dimensional imaging of fission tracks using confocal scanning laser microscopy, *American Mineralogist* 77 (1992) 529–533.
- [21] N. Petford, J. A. Miller, J. Briggs, The automated counting of fission tracks in an external detector by image analysis, *Computers & Geosciences* 19 (4) (1993) 585–591. doi:10.1016/0098-3004(93)90084-I.  
URL <http://linkinghub.elsevier.com/retrieve/pii/009830049390084I>
- [22] G. Espinosa, R. B. Gammage, K. E. Meyer, C. S. Dudley, Nuclear track

- analysis by digital imaging, *Radiation Protection Dosimetry* 66 (1-4) (1996) 363–366.
- [23] A. Boukhair, A. Haessler, J. C. Adlo, A. Nourreddine, New code for digital imaging system for track measurements, *Nuclear Instruments and Methods in Physics Research. Section B, Beam Interactions with Materials and Atoms* 160 (2000) 550–555.
- [24] M. Dolleiser, S. R. Hashemi-Nezhad, A fully automated optical microscope for analysis of particle tracks in solids, *Nuclear Instruments and Methods in Physics Research, Section B: Beam Interactions with Materials and Atoms* 198 (1-2) (2002) 98–107. doi:10.1016/S0168-583X(02)01484-2.
- [25] R. Bedogni, Development of a reader for the routine analysis of CR-39 fast neutron dosimeters: improvement of the dosimetric performance using automatic vision and motion tools, *Radiation Measurements* 36 (1-6) (2003) 239–243. doi:10.1016/S1350-4487(03)00131-8.  
URL <http://linkinghub.elsevier.com/retrieve/pii/S1350448703001318>
- [26] N. Yasuda, K. Namiki, Y. Honma, Y. Umeshima, Y. Marumo, H. Ishii, E. R. Benton, Development of a high speed imaging microscope and new software for nuclear track detector analysis, *Radiation Measurements* 40 (2-6) (2005) 311–315. doi:10.1016/j.radmeas.2005.02.013.
- [27] H. Tawara, K. Eda, K. Takahashi, T. Doke, N. Hasebe, S. Kodaira, S. Ota, M. Kurano, N. Yasuda, Development of an automated multisample scanning system for nuclear track etched detectors, *Nuclear Instruments and Methods in Physics Research, Section A: Accelerators, Spectrometers, Detectors and Associated Equipment* 593 (3) (2008) 475–480. doi:10.1016/j.nima.2008.05.035.
- [28] A. F. de Siqueira, W. M. Nakasuga, A. Pagamisse, C. A. Tello Saenz, A. E. Job, An automatic method for segmentation of fission tracks in epidote

- crystal photomicrographs, *Computers and Geosciences* 69 (2014) 55–61.  
doi:10.1016/j.cageo.2014.04.008.  
URL <http://dx.doi.org/10.1016/j.cageo.2014.04.008>
- [29] J. Ruan, H. Li, J. Zhang, Z. Zhang, L. Chen, J. Song, J. Liu, J. Liu, Image mosaic method for recognition of proton track in nuclear emulsions, *Nuclear Instruments and Methods in Physics Research Section A: Accelerators, Spectrometers, Detectors and Associated Equipment* 762 (2014) 16–21. doi:10.1016/j.nima.2014.05.040.  
URL <http://dx.doi.org/10.1016/j.nima.2014.05.040><http://linkinghub.elsevier.com/retrieve/pii/S0168900214005671>
- [30] E. Enkelmann, T. A. Ehlers, G. Buck, A. K. Schatz, Advantages and challenges of automated apatite fission track counting, *Chemical Geology* 322–323 (2012) 278–289. doi:10.1016/j.chemgeo.2012.07.013.  
URL <http://dx.doi.org/10.1016/j.chemgeo.2012.07.013>
- [31] S. Beucher, C. Lantuejoul, Use of Watersheds in Contour Detection (1979).  
doi:citeulike-article-id:4083187.  
URL <http://www.citeulike.org/group/7252/article/4083187>
- [32] J. Serra, Image analysis and mathematical morphology, Vol. 1, Academic press, 1982.
- [33] F. M. Schaller, M. Neudecker, M. Saadatfar, G. Delaney, K. Mecke, G. E. Schröder-Turk, M. Schröter, Tomographic analysis of jammed ellipsoid packings, in: *AIP Conference Proceedings*, Vol. 1542, 2013, pp. 377–380. doi:10.1063/1.4811946.  
URL <http://aip.scitation.org/doi/abs/10.1063/1.4811946>
- [34] G. H. Ball, D. J. Hall, A clustering technique for summarizing multivariate data, *Behavioral Science* 12 (2) (1967) 153–155. doi:10.1002/bs.3830120210.

- [35] T. W. Ridler, S. Calvard, Picture Thresholding Using an Iterative Selection Method, *IEEE Transactions on Systems, Man and Cybernetics* 8 (8) (1978) 630–632. doi:10.1109/TSMC.1978.4310039.
- [36] F. R. Dias Velasco, Thresholding Using the ISODATA Clustering Algorithm, *IEEE Transactions on Systems, Man, and Cybernetics* 10 (11) (1980) 771–774. doi:10.1109/TSMC.1980.4308400.  
URL <http://ieeexplore.ieee.org/document/4308400/>
- [37] S. van der Walt, J. L. Schönberger, J. Nunez-Iglesias, F. Boulogne, J. D. Warner, N. Yager, E. Goullart, T. Yu, scikit-image: image processing in Python, *PeerJ* 2 (2014) e453. arXiv:1407.6245, doi:10.7717/peerj.453.  
URL <https://peerj.com/articles/453>
- [38] C. Fiorio, J. Gustedt, Two linear time Union-Find strategies for image processing, *Theoretical Computer Science* 154 (2) (1996) 165–181. doi:10.1016/0304-3975(94)00262-2.
- [39] J. C. Russ, *The Image Processing Handbook*, 6th Edition, CRC Press, 2011.  
URL <https://www.crcpress.com/The-Image-Processing-Handbook-Sixth-Edition/Russ/p/book/9781439840450>
- [40] J. F. Ziegler, M. D. Ziegler, J. P. Biersack, SRIM - The stopping and range of ions in matter (2010), *Nuclear Instruments and Methods in Physics Research, Section B: Beam Interactions with Materials and Atoms* 268 (11-12) (2010) 1818–1823. doi:10.1016/j.nimb.2010.02.091.  
URL <http://dx.doi.org/10.1016/j.nimb.2010.02.091>
- [41] S. van der Walt, S. C. Colbert, G. Varoquaux, The NumPy Array: A Structure for Efficient Numerical Computation, *Computing in Science & Engineering* 13 (2) (2011) 22–30. doi:10.1109/MCSE.2011.37.  
URL <http://ieeexplore.ieee.org/document/5725236/>
- [42] E. Jones, T. Oliphant, P. Peterson, *SciPy: Open source scientific tools for*

Python (2001–).

URL <http://www.scipy.org/>

- [43] J. D. Hunter, Matplotlib: A 2D Graphics Environment, *Computing in Science & Engineering* 9 (3) (2007) 90–95. doi:10.1109/MCSE.2007.55.  
URL <http://ieeexplore.ieee.org/document/4160265/>
- [44] G. van Rossum, Python Reference Manual, Tech. rep., Centrum voor Wiskunde en Informatica (CWI), Amsterdam (1995).  
URL <https://ir.cwi.nl/pub/5008/05008D.pdf>
- [45] C. T. Rueden, J. Schindelin, M. C. Hiner, B. E. DeZonia, A. E. Walter, E. T. Arena, K. W. Eliceiri, ImageJ2: ImageJ for the next generation of scientific image data, *BMC Bioinformatics* 18 (1) (2017) 529. doi:10.1186/s12859-017-1934-z.  
URL <https://bmcbioinformatics.biomedcentral.com/articles/10.1186/s12859-017-1934-z>
- [46] S. Guedes, J. C. Hadler, P. J. Iunes, S. R. Paulo, C. A. Tello, On the reproducibility of SSNTD track counting efficiency, *Nuclear Instruments and Methods in Physics Research Section A: Accelerators, Spectrometers, Detectors and Associated Equipment* 418 (2-3) (1998) 429–433. doi:10.1016/S0168-9002(98)00918-8.  
URL <http://linkinghub.elsevier.com/retrieve/pii/S0168900298009188>
- [47] A. J. Hurford, P. F. Green, The zeta age calibration of fission-track dating, *Chemical Geology* 41 (1983) 285–317. doi:10.1016/S0009-2541(83)80026-6.  
URL <http://linkinghub.elsevier.com/retrieve/pii/S0009254183800266>
- [48] A. J. Hurford, Standardization of fission track dating calibration: Recommendation by the Fission Track Working Group of the I.U.G.S. Subcom-

mission on Geochronology, *Chemical Geology: Isotope Geoscience Section* 80 (2) (1990) 171–178. doi:10.1016/0168-9622(90)90025-8.

- [49] C. J. Soares, I. Alencar, S. Guedes, R. H. Takizawa, B. Smilgys, J. C. Hadler, Alpha spectrometry study on LR 115 and Makrofol through measurements of track diameter, *Radiation Measurements* 50 (2013) 246–248. doi:10.1016/j.radmeas.2012.06.010.
- [50] J. C. Hadler, P. J. Iunes, C. A. Tello, F. Chemale, K. Kawashita, E. A. C. Curvo, F. G. S. Santos, T. E. Gasparini, P. A. F. P. Moreira, S. Guedes, Experimental study of a methodology for Fission-track Dating without neutron irradiation, *Radiation Measurements* 44 (9-10) (2009) 955–957. doi:10.1016/j.radmeas.2009.10.081.  
URL <http://dx.doi.org/10.1016/j.radmeas.2009.10.081><http://linkinghub.elsevier.com/retrieve/pii/S1350448709002571>
- [51] N. Hasebe, J. Barbarand, K. Jarvis, A. Carter, A. J. Hurford, Apatite fission-track chronometry using laser ablation ICP-MS, *Chemical Geology* 207 (3-4) (2004) 135–145. doi:10.1016/j.chemgeo.2004.01.007.
- [52] C. J. Soares, S. Guedes, J. C. Hadler, R. Mertz-Kraus, T. Zack, P. J. Iunes, Novel calibration for LA-ICP-MS-based fission-track thermochronology, *Physics and Chemistry of Minerals* 41 (1) (2014) 65–73. doi:10.1007/s00269-013-0624-2.
- [53] C. J. Soares, R. Mertz-Kraus, S. Guedes, D. F. Stockli, T. Zack, Characterisation of Apatites as Potential Uranium Reference Materials for Fission-track Dating by LA-ICP-MS, *Geostandards and Geoanalytical Research* 39 (3) (2015) 305–313. doi:10.1111/j.1751-908X.2014.00301.x.  
URL <http://doi.wiley.com/10.1111/j.1751-908X.2014.00301.x>
- [54] D. J. Gombosi, J. I. Garver, S. L. Baldwin, On the development of electron microprobe zircon fission-track geochronology, *Chemical Geology* 363 (2014) 312–321. doi:10.1016/j.chemgeo.2013.11.005.  
URL <http://dx.doi.org/10.1016/j.chemgeo.2013.11.005>

- [55] A. N. C. Dias, F. Chemale, C. J. Soares, S. Guedes, A new approach for electron microprobe zircon fission track thermochronology, *Chemical Geology* 459 (January) (2017) 129–136. doi:10.1016/j.chemgeo.2017.04.014.  
URL <http://dx.doi.org/10.1016/j.chemgeo.2017.04.014>

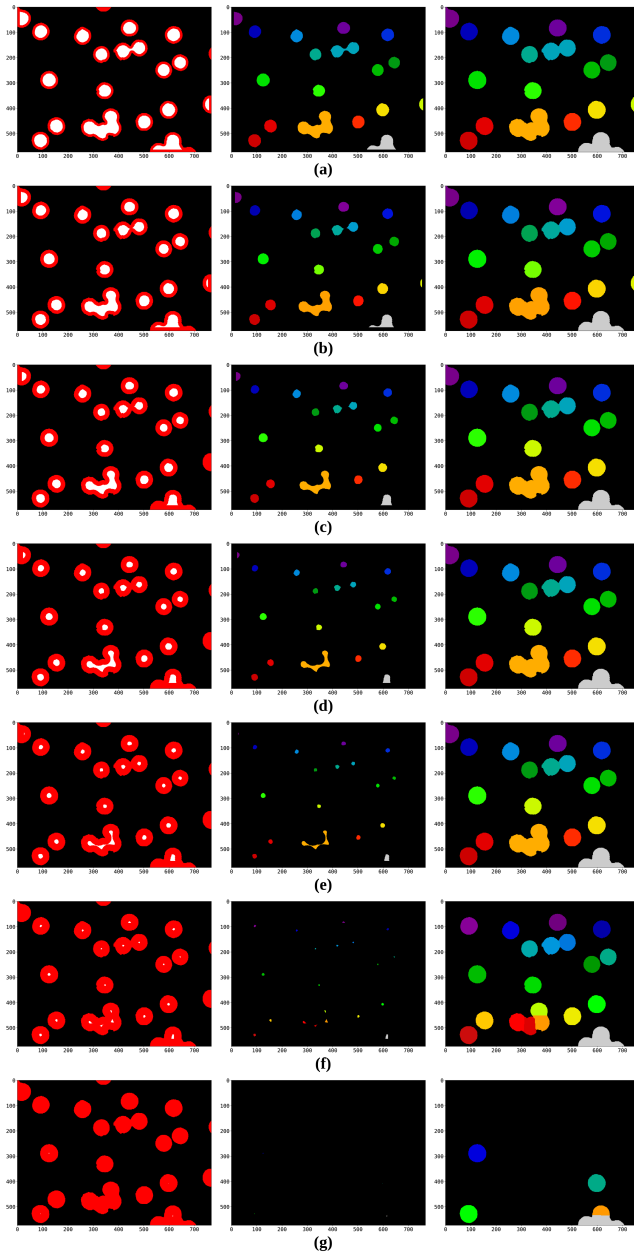


Figure 7: Processing an input image using WUSEM. Each line presents a segmentation step. Left column: original binary image (red) and erosion obtained according to the variation of  $\delta_{radius}$  (white). Center column: erosion results labeled, used as markers. Right column: watershed results when using generated markers. Parameters for WUSEM algorithm:  $\text{initial\_radius} = 10, \delta_{radius} = 4$ .

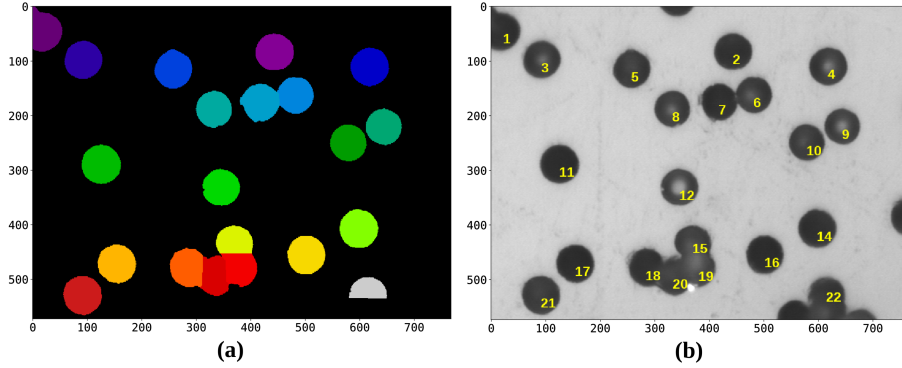


Figure 8: (a) Labels generated from tracks in Figure 4 using the WUSEM algorithm. (b) Tracks in (a) enumerated using `enumerate_objects()`. Tracks in the lower or right corners are not counted, according to the “lower right corner” method. Parameters for WUSEM algorithm: `initial_radius = 10`, `delta_radius = 4`. Colormaps: (a) `nipy_spectral`, (b) `gray`.

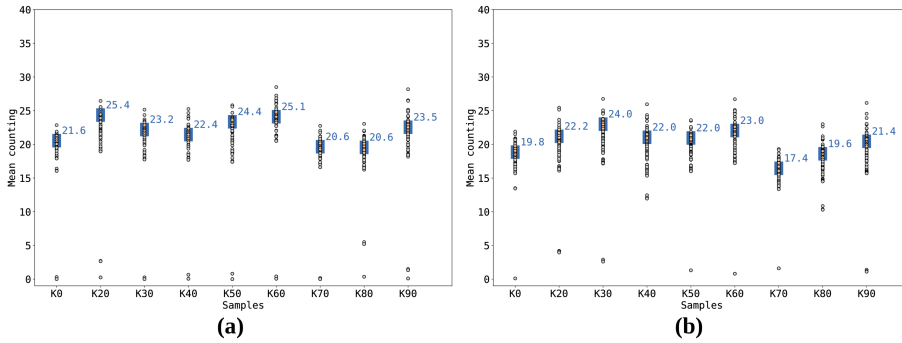


Figure 9: Manual counting mean (top of the blue bar; values on the right) for each sample and automatic counting results with mean within (orange points) and outside (gray points) the tolerance interval (blue bar) for the first dataset.

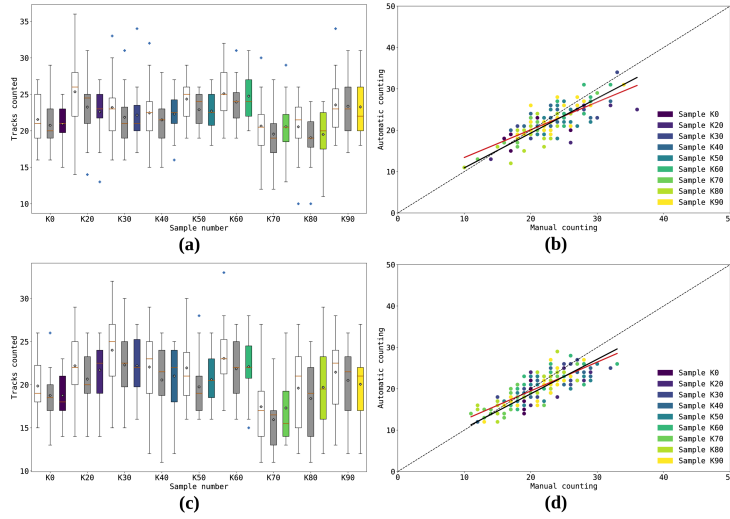


Figure 10: Comparison between manual and automatic counting for (a, b) 4.5 min etching samples and (c, d) 8.5 min etching samples. (a, c) white: manual counting. Gray: flooding watershed counting. Red line: distribution median. White signal: distribution mean. (b, d) dashed: 1:1 line. Red line: regression for the WUSEM counting data. Black line: regression for the flooding watershed counting data.

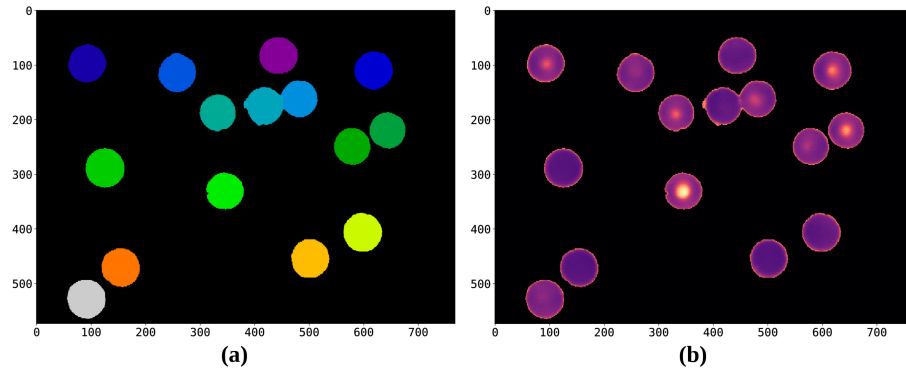


Figure 11: Regions from Figure 4 complying with  $\epsilon \leq 0.3$ . (a) labeled regions. (b) tracks correspondent to (a) in their original gray levels. Colormaps: (a) `nipy_spectral`. (b) `magma`.

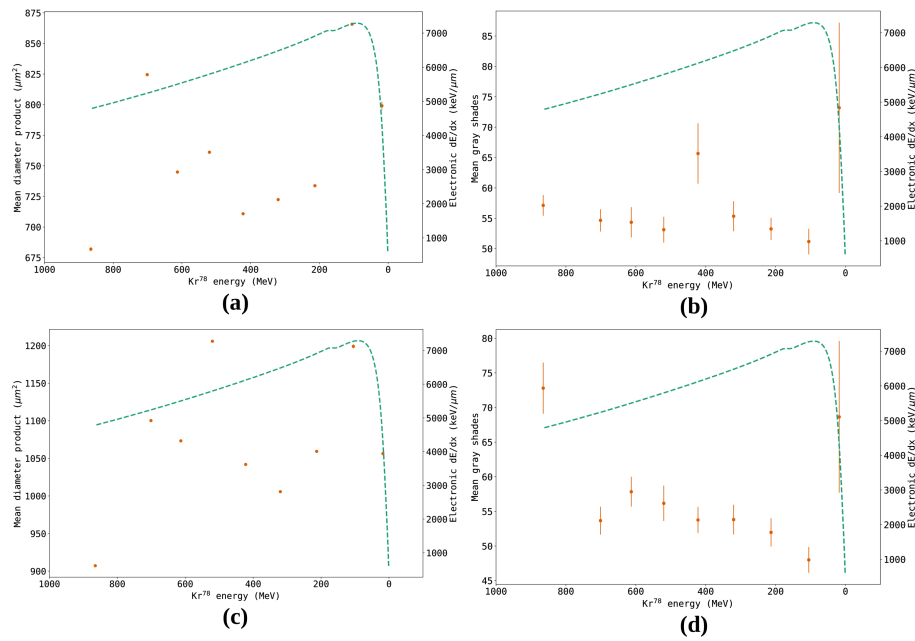


Figure 12: Relation between incident energy versus mean diameter product ((a) 4.5 min; (c) 8.5 min samples, left Y axis) and incident energy versus mean gray levels ((b) 4.5 min; (d) 8.5 min samples, left Y axis). Cyan dashed line: electronic energy loss calculated with SRIM (right Y axis).

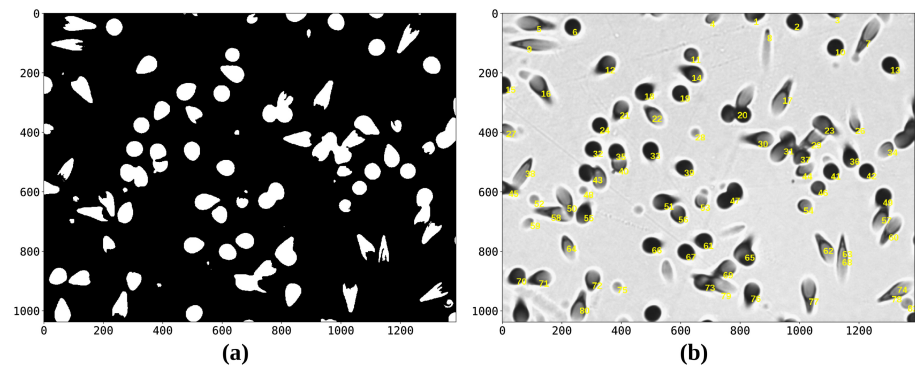


Figure 13: (a) Input photomicrograph (Figure 5) binarized using the ISODATA threshold (threshold = 0.59) and region filling. (b) Tracks separated in Figure 5 using the WUSEM algorithm, and then enumerated using the function `enumerate_objects()`. Parameters for WUSEM algorithm: `initial_radius = 5`, `delta_radius = 12`.

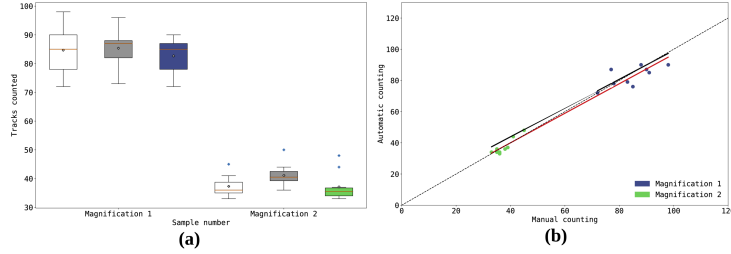


Figure 14: Comparison between manual and automatic counting for photomicrographs in dataset 2. (a) white: manual counting. Gray: flooding watershed counting. Red line: distribution median. White signal: distribution mean. Blue dots: outliers. (b) dashed: 1:1 line. Red line: regression for the WUSEM counting data. Black line: regression for the flooding watershed counting data.

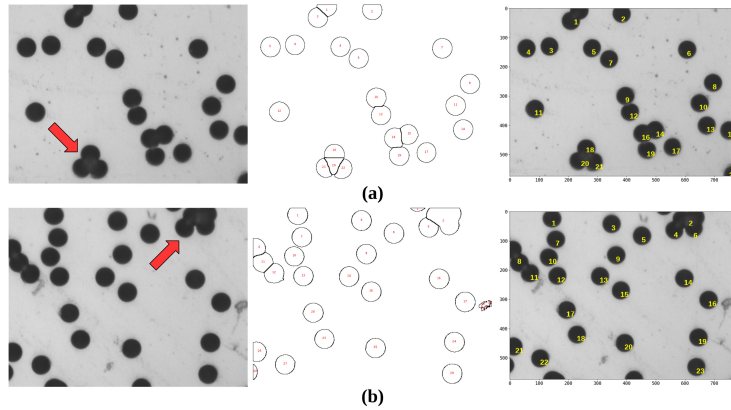


Figure 15: When using suitable input parameters, WUSEM may perform better in certain regions where the classic watershed does not return reliable results. For instance, the highlighted region in (a) presents three tracks. WUSEM separates them correctly, but the region is oversegmented by the classic watershed. The highlighted region in (b), by its turn, is undersegmented by the classic watershed, which returns two tracks. WUSEM returns three tracks, being closer to the real number (four tracks). Left: input photomicrographs with highlighted regions. Center: tracks separated using WUSEM. Right: tracks separated using classic watershed. Parameters for WUSEM algorithm:  $\text{initial\_radius} = 15$ ,  $\text{delta\_radius} = 4$ .